Accuracy of stress measurement by Laue microdiffraction (Laue-DIC method): the influence of image noise, calibration errors and spot number

F. G. Zhang,[a,b] M. Bornert,[c] J. Petit[d] and O. Castelnau[a]*

[a]PIMM CNRS UMR 8006, Arts et Métiers ParisTech, 151 Boulevard de l'Hôpital, 75013 Paris, France, [b]State Key Laboratory of Metal Matrix Composites, Shanghai Jiao Tong University, 800 Dongchuan Road, 200240 Shanghai, People's Republic of China, [c]Laboratoire NAVIER, ENPC/IFSTTAR/CNRS UMR 8205, Université Paris-Est, 77455 Marne-la-Vallée, France, and [d]LEME CNRS EA 4416, Université Paris-Ouest, 50 rue de Sèvres, 92410 Ville d'Avray, France. *Correspondence e-mail: olivier.castelnau@ensam.eu

Keywords: Laue microdiffraction; image noise; digital image correlation; stress analysis.

Laue microdiffraction, available at several synchrotron radiation facilities, is well suited for measuring the intragranular stress field in deformed materials thanks to the achievable submicrometer beam size. The traditional method for extracting elastic strain (and hence stress) and lattice orientation from a microdiffraction image relies on fitting each Laue spot with an analytical function to estimate the peak position on the detector screen. The method is thus limited to spots exhibiting ellipsoidal shapes, thereby impeding the study of specimens plastically deformed. To overcome this difficulty, the so-called Laue-DIC method introduces digital image correlation (DIC) for the evaluation of the relative positions of spots, which can thus be of any shape. This paper is dedicated to evaluating the accuracy of this Laue-DIC method. First, a simple image noise model is established and verified on the data acquired at beamline BM32 of the European Synchrotron Radiation Facility. Then, the effect of image noise on errors on spot displacement measured by DIC is evaluated by Monte Carlo simulation. Finally, the combined effect of the image noise, calibration errors and the number of Laue spots used for data treatment is investigated. Results in terms of the uncertainty of stress measurement are provided, and various error regimes are identified.

1. Introduction

Many natural and engineering materials, such as glass, concrete, steel, plastics, *etc*., have a heterogeneous structure at a certain level of observation (Nguyen *et al.*, 2011). Material scientists have long been aware that many macroscopic phenomena originate from the mechanics of the underlying microstructure, and the insight of material behavior at the microscale is necessary for predicting the macroscopic mechanical response of material. Thanks to the development of synchrotron radiation, bright and stable X-ray sources with beam sizes inferior to 1 µm are nowadays routinely available. These sources have proved to be very powerful in revealing the material properties at the micrometer scale (Barabash *et al.*, 2001; Tamura *et al.*, 2002; Ferrié *et al.*, 2005), *i.e.* in many polycrystalline materials at a subgranular scale.

Stress measurement at the micrometer scale can be realised by either monochromatic or white X-ray beam. In monochromatic beam mode, the specimen needs to be rotated relative to the incoming beam so that a series of diffraction peaks can be recorded according to Bragg's law,

$$\lambda = 2d_{hkl}\sin\theta, \tag{1}$$

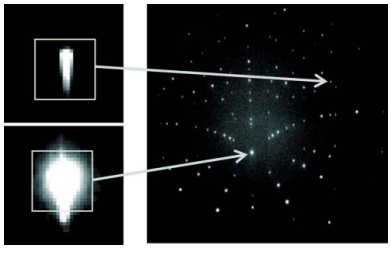

with θ the scattering angle, λ the wavelength of the diffracted X-ray and d_{hkl} the lattice spacing of the diffracted planes whose Miller index is (*hkl*). However, since the overall sphere of confusion of goniometers is rarely better than 30 μm (three sample rotations are needed for single-crystal diffraction), a micrometer spatial resolution can hardly be achieved (Castelnau *et al.*, 2001; Ungár *et al.*, 2007) with monochromatic beam. Alternatively, by using white beam one can record simultaneously a group of Laue spots on an area detector (see Fig. 1) without any rotation and obtain a Laue microdiffraction image (LMDI). In that case, the spatial resolution of the setup is no longer limited by the sphere of confusion but determined by the size of the beam and its penetration depth. Beamline BM32 installed at the European Synchrotron Radiation Facility (ESRF) offers white beam with size inferior to 500 nm × 500 nm and a flat energy spectrum ranging from 5 keV to 22 keV (Ulrich *et al.*, 2011). Routinely, Laue microdiffraction allows the deviatoric part of the elastic strain tensor to be estimated; the trace of elastic strain can by determined by using an additional energy-dispersive detector (Robach *et al.*, 2011) or the rainbow technique (Robach *et al.*, 2013). In this paper, we are only concerned with the determination of the deviatoric strain.

The traditional method for obtaining elastic strain/stress and lattice orientation from LMDI has been elaborated by Chung & Ice (1999). The precision of this method depends on (i) the determination of the diffraction peak position and (ii) the calibration of the experimental setup (see Appendix *A*). Mainstream open-source codes, such as *XMAS* (Tamura, 2014) and *LaueTools* (http://sourceforge.net/projects/laue tools/), usually locate the diffraction peak by fitting the distribution of gray levels of a spot with Gaussian, Lorentzian or Pearson functions, of which the Lorentzian function is said to give the best estimation of the diffraction peak (Valek, 2003). These fittings implicitly assume the ellipticity of the shape of the Laue spot. However, such ellipticity can hardly be guaranteed in many cases; for example, if the crystal contains dislocations, the diffracted spots would be streaked or even split (Barabash *et al.*, 2001; Ohashi *et al.*, 2009), or, if there existed a strain gradient within a pure crystal, the diffracted spots would be accompanied by mirage spots due to dynamic effects (Yan & Noyan, 2006). This issue limits the credibility of stresses inferred from Laue microdiffraction. It is estimated that the accuracy of peak position by fitting is ∼0.1 pixel for a spot of good quality (Poshadel *et al.*, 2012), which corresponds to a precision of ∼10 MPa in the stress for steels with the setup configuration routinely used at ESRF beamline BM32 (Petit *et al.*, 2015). In fact, the traditional method may sometimes give unrealistic results when the grain has undergone significant plastic strain and stored a significant density of dislocations. For example, the residual shear stress within a Cu monocrystal estimated by traditional methods reached 1 GPa, much higher than its yield stress (Magid *et al.*, 2009).

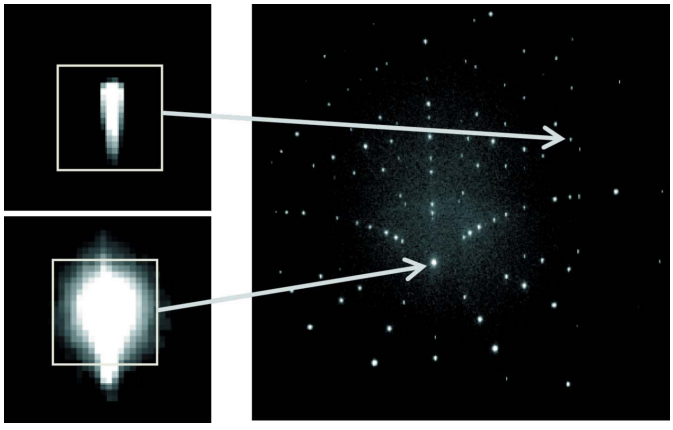

Figure 1
Typical Laue microdiffraction image obtained from a Si single-crystal (Petit *et al.*, 2015). The rectangle around a Laue spot represents the correlation window used for DIC.

A method called Laue-DIC was proposed to bypass this issue (Petit *et al.*, 2015). The novelty of Laue-DIC is that it no longer locates the peak positions by fitting on each individual image; instead, it measures the displacements of peaks between two diffraction images by digital image correlation (DIC). In the experiment carried out at ESRF beamline BM32, it was demonstrated that the precision of elastic strain increment between two images could be of the order of 10^{-5} with Laue-DIC, corresponding to a stress resolution of 2 MPa for steel.

Although Laue-DIC has demonstrated its potential in resolving intragranular stress fields, one should be aware that the resolution of Laue-DIC is also limited by various factors, notably the DIC errors (Wang *et al.*, 2009; Bornert *et al.*, 2009), calibration errors (Hofmann *et al.*, 2011; Poshadel *et al.*, 2012) and the number of Laue spots considered in the images. This paper is dedicated to investigating the influence of these factors. It is structured as follows: first, a brief introduction of Laue-DIC is given in §2; then a simple procedure for characterizing the image noise is applied in §3; next, we propose a framework of Monte Carlo simulation to analyze the transmission of image noise to the errors of peak displacements by DIC in §4; the DIC errors estimated with the aforementioned method, together with the calibration errors, are further fed into another Monte Carlo simulation to estimate the errors of stress measurement in §5, and this method is applied to the analysis of the stress profiles of a bent monocrystal; finally we use the established Monte Carlo simulation procedure to investigate the collective effect of the aforementioned factors on the accuracy of the Laue-DIC method in §6.

2. Laue-DIC

2.1. Brief introduction of DIC

DIC belongs to the category of optical full-field measurement techniques. Compared with other optical techniques, *e.g.* photoelasticity, moiré, holography, speckle interferometry, grid method, *etc.*, the procedure of DIC is more straightforward and simple. It originates from the research activities in artificial intelligence and robotics to develop vision-based algorithms and stereo-vision methodologies in parallel with photogrammetry applications for aerial photographs (Sutton

et al., 2009). However, gradually, it lent its application to the realm of mechanics, because it offers a non-contact and non-destructive method to measure materials' kinematic fields (Yamaguchi, 1981; Peters & Ranson, 1982; Wattrisse *et al.*, 2001; Abanto-Bueno & Lambros, 2002; Wang & Cuitiño, 2002; Bergonnier *et al.*, 2005).

The procedure of DIC consists of recording several digital images of a specimen during its deformation and comparing these images two by two with an image correlation algorithm. The image correlation technique matches subsets in the series of images to provide a measurement of the displacement field. Thanks to the constant decrease of costs of digital cameras and computers, this method is becoming increasingly available to both industry and academic society.

To determine the displacement field between two images, one needs to designate in the first image a set of rectangular sub-images (of size typically 20×20 pixels) referred to as the *correlation windows*. Each correlation window finds its counterpart in the second image by minimizing a correlation coefficient which quantifies the resemblance of two correlation windows. The simplest form of correlation coefficient is defined by the sum of squared difference (SSD),

$$C_{\mathrm{SSD}} \doteq \sum \left\{ f(\mathbf{x}) - g\left[\boldsymbol{\Phi}(\mathbf{x})\right] \right\}^2, \tag{2}$$

where the sum runs over all pixels in the correlation window, $\mathbf{x}$ is the pixels' positions in the correlation window, the functions f and g provide the gray level at a given position in two correlation windows, respectively, and $\boldsymbol{\Phi}$ is the so-called 'shape function' which defines the mechanical transformation of the correlation window. Therefore, $\boldsymbol{\Phi}$ can be associated with rigid-body displacements, rigid-body rotations and deformation (possibly heterogeneous) of the correlation window, for which an analytical generic expression is chosen; here, only rigid-body translation will be considered. The ultimate purpose of DIC is to determine the coefficients of the shape function $\boldsymbol{\Phi}$.

In the *CMV* software, the in-house DIC tool used in this work (Doumalin & Bornert, 2000; Bornert *et al.*, 2010), a zero-mean normalized cross correlation (ZNCC) coefficient is used,

$$C_{\mathrm{ZNCC}} \doteq 1 - \frac{\sum \left[f(\mathbf{x}) - \overline{f} \right] \left\{ g\left[\boldsymbol{\Phi}(\mathbf{x})\right] - \overline{g} \right\}}{\left(\sum \left[f(\mathbf{x}) - \overline{f} \right]^2 \sum \left\{ g\left[\boldsymbol{\Phi}(\mathbf{x})\right] - \overline{g} \right\}^2 \right)^{1/2}}, \tag{3}$$

where $\overline{f}$ and $\overline{g}$ are the averages of $f(\mathbf{x})$ and $g[\boldsymbol{\Phi}(\mathbf{x})]$ over the window, respectively. Compared with other forms of correlation coefficients, ZNCC is insensitive to the offset and scale changes in the gray level of the image (Tong, 2005). The property is useful when the image acquisition procedure cannot guarantee the strict conservation of gray levels, such as for scanning electron microscopy images (Doumalin & Bornert, 2000).

2.2. Procedure and formulation of Laue-DIC

Here we briefly introduce the procedure of Laue-DIC (Petit *et al.*, 2015). To begin with, we need to define a lattice matrix, whose columns are the components of the three lattice vectors $\mathbf{a}$, $\mathbf{b}$, $\mathbf{c}$, of a crystal. Here, the lattice matrix is denoted by the capital letter $\mathbf{M}$. From the lattice matrix and the calibration parameters (denoted by $\mathcal{C}$; see Appendix *A*) of the diffraction setup, one can uniquely determine the peak position of the Laue spot, say $\mathbf{X}^{hkl}$, on the detector screen corresponding to the lattice plane (*hkl*),

$$\mathbf{X}^{hkl} = f(\mathbf{M}, \mathcal{C} \,|\, hkl). \tag{4}$$

Let us designate the strain-free lattice (*i.e.* the undeformed lattice) as the *reference lattice* and denote its lattice matrix as $\mathbf{M}_0$. When the lattice has deformed (state designated as *current lattice*), the lattice spacing d_{hkl} of equation (1) alters together with the normal direction of the (*hkl*) plane, and hence the associated diffraction peak position. The displacement field of Laue spots before and after the deformation can be captured by DIC,

$$\delta\mathbf{X}^{hkl} = \mathbf{X}^{hkl} - \mathbf{X}_0^{hkl}, \tag{5}$$

where the subscript '0' refers to the reference Laue pattern. Assuming that the experimenter has managed to keep constant the calibration parameters during the experiment (*i.e.* $\mathcal{C}$ remains unchanged) and restricting the analysis to the cases in which the two lattices differ by only small elastic strain and small lattice rotation, $\delta\mathbf{X}^{hkl}$ can be expressed with good accuracy by the first-order expansion of function f,

$$\begin{aligned} \delta\mathbf{X}^{hkl} &= \mathbf{X}^{hkl} - \mathbf{X}_0^{hkl} \\ &= f(\mathbf{M}, \mathcal{C} \,|\, hkl) - f(\mathbf{M}_0, \mathcal{C} \,|\, hkl) \\ &\approx \frac{\partial f}{\partial M_{ij}} (\mathbf{M}_0, \mathcal{C} \,|\, hkl)\, \delta M_{ij}, \end{aligned} \tag{6}$$

with $\delta\mathbf{M} = \mathbf{M} - \mathbf{M}_0$ and with implicit summation over indices i and j. $\partial f / \partial M_{ij}$ on the right-hand side of equation (6) can be calculated explicitly, therefore equation (6) linearizes the relationship between $\delta\mathbf{X}^{hkl}$ and $\delta\mathbf{M}$. As explained above, only eight independent components of $\delta\mathbf{M}$ can be assessed by white-beam Laue microdiffraction (the volume change of the lattice, given by the determinant of $\mathbf{M} \cdot \mathbf{M}_0^{-1}$, cannot be measured). Therefore, these eight independent components can be obtained by linear regression if at least four Laue spots' displacements are known. The deformation gradient between the reference and current lattice is given by

$$\mathbf{F} = \mathbf{1} + \delta\mathbf{M} \cdot \mathbf{M}_0^{-1}, \tag{7}$$

with $\mathbf{1}$ being the second-order identity tensor. The expression of $\mathbf{F}$ in the case of small strain $\boldsymbol{\varepsilon}$ and rotation $\boldsymbol{\omega}$ is simply

$$\mathbf{F} = \mathbf{1} + \boldsymbol{\varepsilon} + \boldsymbol{\omega}, \tag{8}$$

where $\boldsymbol{\varepsilon}$ and $\boldsymbol{\omega}$ are the symmetric and asymmetric parts of $\delta\mathbf{M} \cdot \mathbf{M}_0^{-1}$, respectively. To sum up, Fig. 2 presents the flowchart of Laue-DIC.

3. Characterization of image noise

3.1. Noise model

As shown in Fig. 2, the input of the calculation of Laue-DIC is the displacements provided by DIC, therefore the error of DIC would eventually contribute to the error of Laue-DIC.

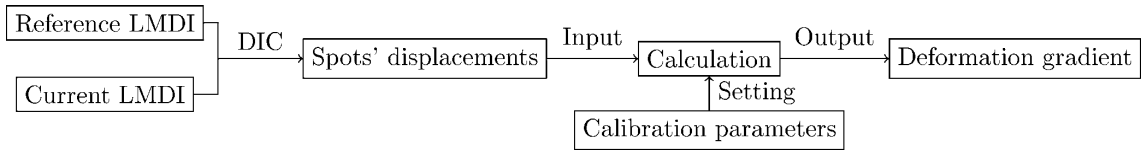

Figure 2
Flowchart of Laue-DIC.

The DIC errors are highly associated with the image noise (Wang *et al.*, 2009; Bornert *et al.*, 2009; Amiot *et al.*, 2013). The detector used in our experiment was an X-ray 11 Mpixel VHR (very high resolution) camera especially customized for BM32 ESRF by Photonic Science, with a 12-bit dynamic. This detector uses a charge-coupled device (CCD) to record signals: the front of the detector is covered by a layer of fluorescent material known as the phosphor screen or scintillator; the incident X-ray photons hitting the scintillator will trigger visible light photons, then these visible light photons travel through optical fibers until detected by the CCD, and finally digitalized into gray level of each pixel (He, 2009).

A wealth of literature has been devoted to investigate the noise of CCD detectors (Arndt & Gilmore, 1979; Stanton *et al.*, 1992; Ponchut, 2006; Waterman & Evans, 2010). Their discussions cover all the steps of an image formation and any possible source of noise. However, since these details go beyond the scope of this paper, we will skip them and provide a simple and concise deduction of a Poissonian–Gaussian noise model for our CCD images.

First, the arrival of a photon in the scintillator of the detector is modeled as a Poisson process, *i.e.* the arrival of a photon is independent of the previous arrivals (Arndt & Gilmore, 1979; Stanton *et al.*, 1992; Waterman & Evans, 2010). Then the probability that n photons arrive at the scintillator during the exposure time would be

$$P(n) = \frac{\exp(-\overline{n})\,\overline{n}^{n}}{n!}, \tag{9}$$

where $\overline{n}$ is both the expectation (represented by $\mathrm{E}[\cdot]$) and the variance (represented by $\mathrm{VAR}[\cdot]$) of the number of arrivals during the exposure time (for a Poisson distribution the expectation equals the variance), *i.e.*

$$\mathrm{E}[n] = \mathrm{VAR}[n] = \overline{n}. \tag{10}$$

If the same exposure process is repeated many times, according to the central limit theorem the distribution of photon number received by the detector pixel can be described by a normal distribution (denoted as $\mathcal{N}$), whose variance and expectation are both $\overline{n}$,

$$n \simeq \mathcal{N}(\overline{n}, \overline{n}). \tag{11}$$

The incident X-ray photons are eventually converted into the gray level of a pixel with the so-called *gain*, defined as 'the ratio of the integrated image signal to the corresponding integrated signal at the detector input' (Ponchut, 2006). In our case, the integrated image signal is the gray level (expressed by p_s, where the subscript 's' represents the signal) and the input integrated signal is the accumulation of X-ray photons (n),

$$p_\mathrm{s} = \gamma n, \tag{12}$$

where γ is the gain of the detector. Then the expectation and variance of gray level would be

$$\begin{aligned} \mathrm{E}\big[p_\mathrm{s}\big] &= \mathrm{E}[\gamma n] = \gamma \mathrm{E}[n] = \gamma \overline{n}, \\ \mathrm{VAR}\big[p_\mathrm{s}\big] &= \mathrm{VAR}[\gamma n] = \gamma^2 \mathrm{VAR}[n] = \gamma^2 \overline{n}. \end{aligned} \tag{13}$$

Denoting $\mathrm{E}[p_\mathrm{s}]$ as $\overline{p}_\mathrm{s}$, the variance of the gray level would be $\mathrm{VAR}[p_\mathrm{s}] = \gamma\overline{p}_\mathrm{s}$; then the gray level p_s obeys the following normal distribution,

$$p_\mathrm{s} \simeq \mathcal{N}(\overline{p}_\mathrm{s}, \gamma\overline{p}_\mathrm{s}). \tag{14}$$

Unfortunately, the gray level is also contaminated by the noises inherent to the detector, expressed by p_d, where the subscript 'd' represents the detector. The noise inherent to the detector is usually modeled by a normal distribution. We denote the expectation and variance of this noise with $\overline{p}_\mathrm{d}$ and σ_d^2, *i.e.*

$$\mathrm{E}[p_\mathrm{d}] = \overline{p}_\mathrm{d}, \qquad \mathrm{VAR}[p_\mathrm{d}] = \sigma_\mathrm{d}^2. \tag{15}$$

Various factors contribute to this type of noise, notably the *dark signal* and *digitalization noise*. Dark signal is defined as the non-zero signal at output when the input signal is zero. The dark signal usually results from the thermally produced electron–hole pairs on the CCD chip, and accumulates with the exposure time (Ponchut, 2006; He, 2009); to minimize this phenomenon, the CCD chip should be cooled down. The digitalization noise is introduced in the analog-to-digital conversion of the signal.

Then the overall gray level p, which is believed to be a combination of p_s and p_d, would comply with the following normal distribution,

$$p \simeq \mathcal{N}\big(\overline{p}_\mathrm{s} + \overline{p}_\mathrm{d}, \gamma\overline{p}_\mathrm{s} + \sigma_\mathrm{d}^2\big). \tag{16}$$

Denoting the expectation and the variance of the overall gray level by $\overline{p}$ and σ^2, respectively, *i.e.*

$$\overline{p} = \overline{p}_\mathrm{s} + \overline{p}_\mathrm{d}, \qquad \sigma^2 = \gamma\overline{p}_\mathrm{s} + \sigma_\mathrm{d}^2, \tag{17}$$

we have

$$\sigma^2 = \gamma\overline{p} + \big(\sigma_\mathrm{d}^2 - \overline{p}_\mathrm{d}\gamma\big), \tag{18}$$

where γ, $\overline{p}_\mathrm{d}$ and σ_d^2 are the parameters of this noise model.

3.2. Validation of the noise model by repetitive tests

Let us now identify the noise model with data. Several repetitive tests were carried out to validate the noise model and identify its parameters. A stack of 100 LMDIs was used in each test. During the acquisition of each image stack, we endeavored to maintain strictly the experimental setup to ensure that the only factor leading to the variation of gray

levels from one image to the other ones would be the noise. For each pixel we have calculated the average and standard variance of its gray levels, using all images of the stack.

Although diffraction images (see Fig. 1, for example) acquired from experiments contain huge amounts of pixels (in our case, there are 2594 × 2774 pixels in a single image), only a small portion of pixels, those constituting Laue spots, are of interest. Only these pixels contain information about the specimen, and gray levels significantly differ from the background noise. Therefore, a data reduction process is necessary to isolate these pixels. A rectangular window containing pixels belonging to an individual Laue spot is determined. Since the sizes and the shapes of Laue spots vary according to the spots' energies, angular projection, crystal defects, *etc.*, one needs to adaptively select the windows' sizes to best fit the spots. The data reduction process adopted in this work is shown in Fig. 3, and two subimages of spots obtained by this process are shown in Fig. 4.

Let us now look at an image stack collected from a Si monocrystalline specimen. As the gain of the detector may depend on the energy of the incoming X-rays, we first isolate a subset of pixels which have received X-rays of the same energy. This can be achieved by using pixels belonging to a given Laue spot on the LMDI, selected by the process indicated in Fig. 3. In Fig. 5(*a*) the average gray levels of those pixels are plotted against the corresponding variances of gray levels. The figure indicates a linear relationship between the average and the variance of gray level, as revealed by equation (18). The slope of the linear relation is an estimation of the gain γ, while the interception with the y-axis is an estimation of $\sigma_d^2 - \overline{p}_d\gamma$. Those two parameters are identified by a linear regression on the data points; this leads to a large linear correlation coefficient ($\sim$0.9), thereby confirming the soundness of equation (18).

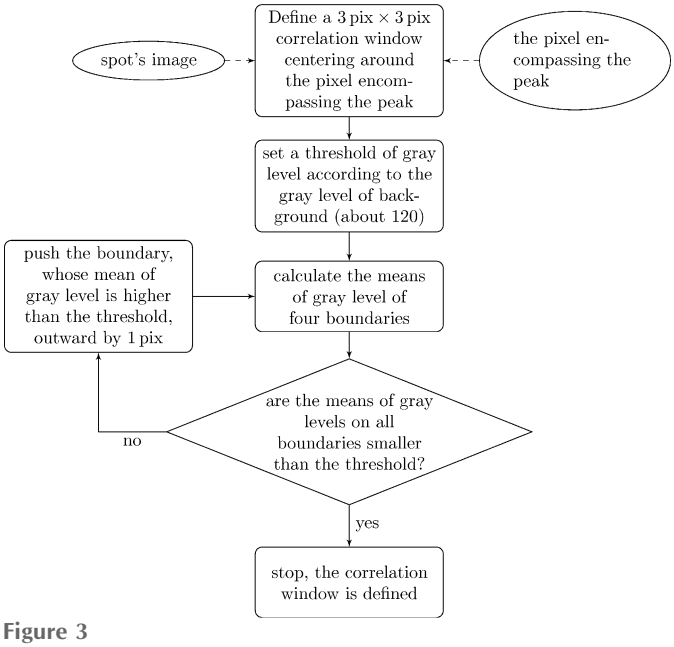

Figure 3
Data reduction process to determine the optimum rectangular window containing a Laue spot.

We have then applied the same procedure to all Laue spots of the LMDI for Si, *i.e.* corresponding to various X-ray energies, and for each spot an estimation of γ and $\sigma_d^2 - \overline{p}_d\gamma$ can be made. Then, plotting the estimated values of γ *versus*

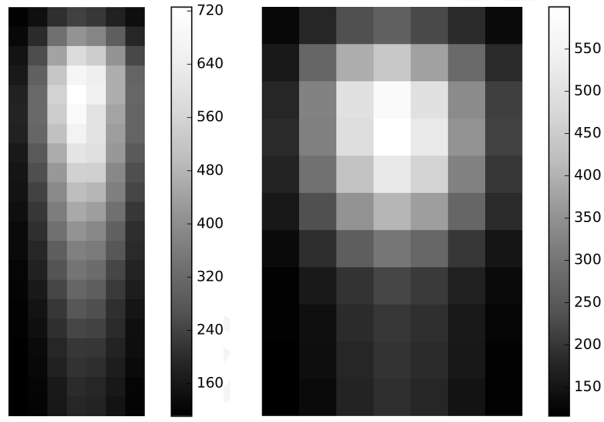

Figure 4
Two subimages of spots obtained by the algorithm in Fig. 3.

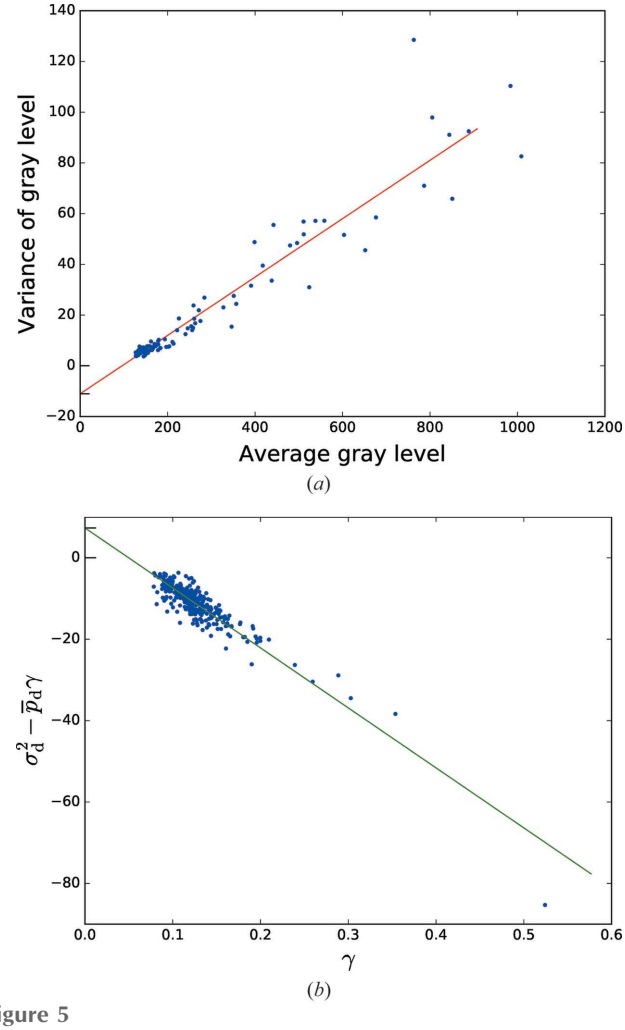

Figure 5
(*a*) Average *versus* variance of gray levels for pixels corresponding to a specific spot obtained on a Si specimen. (*b*) Plot of γ *versus* ($\sigma_d^2 - p_d\gamma$) of all Laue spots of the LMDIs measured on Si, Ge, Cu and Fe specimens.

$(\sigma_d^2 - \overline{p}_d\gamma)$ for all Laue spots enables us to estimate σ_d^2 and $\overline{p}_d$ by another linear regression (figure not shown for conciseness). We found a linear correlation coefficient of -0.94, indicating a high linear correlation, further confirming the soundness of the noise model. The obtained parameters are found to be $\overline{p}_d = 118.7$ and $\sigma_d^2 = 4.3$. The estimated value for $\overline{p}_d$ is slightly larger than the average gray level of the background of the image (about 101.1). We are not clear about this feature. After all, the transmission of signal from incident photons to digital images is too complex to be fully described by a simple Poissonian–Gaussian model. Fortunately, the result of DIC is unaffected by $\overline{p}_d$ as long as the zero-mean normalized cross-correlation (ZNCC) coefficient is used (Tong, 2005), and assuming that $\overline{p}_d$ is homogeneously distributed among all pixels of the detector. Note that the estimated value of γ is not unique as it ranges between $\sim$0.1 and $\sim$0.15.

More data points would give a better estimation of the background noise parameters, *i.e.* $\overline{p}_d$ and σ_d^2. The detector, as an apparatus to detect photons, is ignorant about the diffracting material. Therefore, we further applied the same procedure to image stacks collected from other samples: Ge, Cu and austenitic steel (Fig. 5*b*). This led to a total number of 316 spots investigated. Those image stacks behave similarly to that for Si, exhibiting a strong correlation between the variance and the average of gray levels, as illustrated in Fig. 5(*b*). This led to the following estimation for the noise model parameters: $\overline{p}_d = 147.3$ and $\sigma_d^2 = 7.3$. The estimated $\overline{p}_d$ was again larger than the mean background of the image ($\sim$100). Note again that the gain was not uniquely defined. In Appendix *B*, the effect of X-ray energy on detector gain is investigated. As no clear effect is found, we consider in the following the mean value $\gamma = 0.125$.

In summary, the proposed Poissonian–Gaussian noise model is a simple model but still in good agreement with our data. As we want to investigate the transmission of image noise on the DIC errors, such a noise model consistent with the main data characteristics is sufficient to reach our goal.

4. Impact of image noise on the accuracy of DIC

4.1. Methodology

In this section, we investigate the propagation of image noise on the accuracy of DIC by Monte Carlo simulation. In previous work (Petit *et al.*, 2015), the DIC errors for LMDIs have been investigated experimentally using the displacement of a Ge single-crystal in a direction parallel to the incident beam. At each specimen position, a LMDI was acquired, and the correlation between all images should in principle result in a uniform displacement of all Laue spots by the same amount as the displacement prescribed to the specimen. Deviation from this prescribed displacement reflected the error of DIC. The mean systematic errors were found to be small, $\sim$0.018 pixels (for a MAR CCD detector, with a pixel size of 80.6 μm). A drawback of this procedure comes from the fact that it also integrates some experimental errors (assumed to remain small but hardly checkable) as the specimen needs to be translated exactly along the beam direction; any deviation from the perfect movement would be interpreted as DIC error when using this procedure. The real DIC errors should thus be smaller than those estimated by Petit *et al.* (2015).

Another possible approach consists of transforming numerically a real Laue image to a known displacement field. The transformation is accomplished either in the frequency domain by applying Fourier transformation or in the space domain by interpolating at subpixel positions. Although this approach can retain all characteristics of images taken under experimental conditions, the numerical transformation itself introduces some errors (Bornert *et al.*, 2017) depending on the specific algorithm used.

In this work, we avoid using real images for the sake of the issue mentioned above. The DIC errors were instead estimated on synthetic images of a Laue spot. In fact, it is the gray-level gradient within the rectangular window containing the spot that determines the precision of DIC (Wang *et al.*, 2009; Bornert *et al.*, 2009; Amiot *et al.*, 2013). Therefore, if the gray-level gradient of a synthesized spot is representative of that of a real spot, we can anticipate a fair assessment of the DIC result. In our approach, the intensity distribution of a synthesized spot is modeled by a two-dimensional Gaussian function,

$$\begin{aligned} I(x,y) &= A\exp\left\{-\left[C_1(x-x_0)^2 + C_2(x-x_0)(y-y_0)\right.\right. \\ &\quad \left.\left. + C_3(y-y_0)^2\right]\right\} + \overline{p}_d, \\ C_1 &= \left(\cos^2\theta/r_X^2 + \sin^2\theta/r_Y^2\right)/2, \\ C_2 &= \sin\theta\cos\theta\left(-1/r_X^2 + 1/r_Y^2\right), \\ C_3 &= \left(\sin^2\theta/r_X^2 + \cos^2\theta/r_Y^2\right)/2, \end{aligned} \tag{19}$$

where A represents the amplitude of the spot, x_0 and y_0 represent the center of the spot, r_X and r_Y are the widths of the spot along the two main axes at the $1/\sqrt{e}$ of the maximum height, θ represents the rotation angle of the main axes of the Gaussian function with respect to the pixel grid, and $\overline{p}_d$ is the dark signal mentioned in §3.1.

The calculation of the reference image first required integration of equation (19) within each image pixel. Then, the gray level of each pixel was provided by the nearest integer value of the integral. As for the synthesis of the displaced spots (current image), a so-called multi-resolution approach (Doumalin & Bornert, 2000) was employed. It works as follows:

(i) Subdivide each pixel into $N \times N$ subpixels. N will represent the resolution of subpixel step.

(ii) Calculate the gray level for each subpixel by integration of equation (19) within each subpixel.

(iii) To obtain the gray level of each pixel after a displacement of i/N pixels along the x direction and j/N pixels along the y direction, where i and j are integers smaller than N, one only has to move the pixel by i and j substeps, as depicted in Fig. 6. Then, we bin subpixels together within the moved pixel, and take the nearest integer value to obtain its gray level.

Here, we chose the sample size N to be 100, then the resolution of the subpixel displacement was 0.01 pixel. Fig. 7

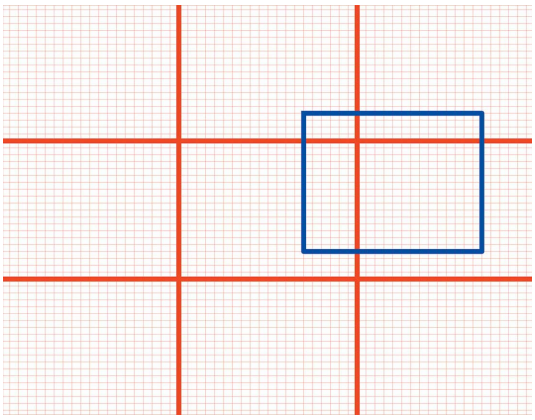

Figure 6
The red thick squares represent 3×3 pixels subdivided into $N \times N$ subpixels, and the blue square represents the central pixel after being moved by a subpixel displacement.

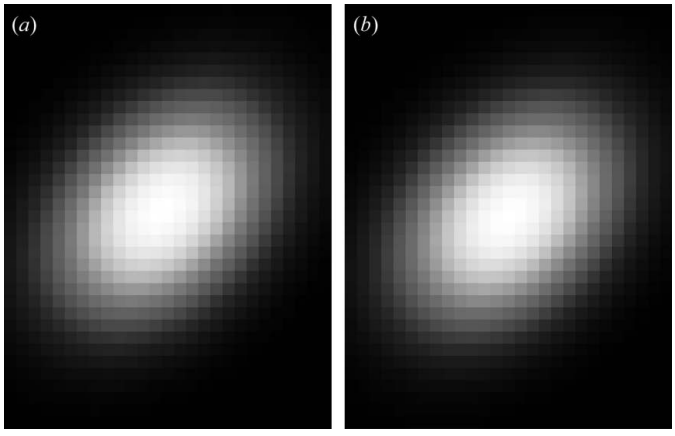

Figure 7
A synthetic Laue spot before and after displacement. (*a*) Initial spot. (*b*) After being moved by 0.5 pixel along each direction. The shapes of the spots are determined by the following parameters: A = 114.43, r_X = 6.39 pixel, r_Y = 4.51 pixel, $\theta = 45°$.

depicts a spot before and after a subpixel displacement of 0.5 pixel along both the x and y directions as examples.

4.2. Error estimation

We implemented the above-mentioned procedure using the in-house DIC code *CMV* (Doumalin & Bornert, 2000; Bornert *et al.*, 2010). The parameters characterizing the spot used for this study are tabulated in Table 1, which come from analytically fitting a real spot.

Let us first study the case where image noise is absent. The Laue spot is moved by i/N pixel and j/N pixel along directions x and y as described above, and the error between the imposed displacement and that obtained by DIC is calculated as

$$e_x = x_{\text{dic}} - x_{\text{imposed}}, \qquad e_y = y_{\text{dic}} - y_{\text{imposed}}. \tag{20}$$

Fig. 8 depicts the distributions of both errors, e_x and e_y, as functions of the two-dimensional subpixel displacement between 0 and 1 pixel.

Table 1
Parameters used for Laue spot generation.

A	r_X (pixel)	r_Y (pixel)	θ
572.65	2.54	1.75	173.18°

It shows that error e_x essentially depends on displacement along direction x, and e_y essentially depends on displacement along direction y. In other words, error e_x poorly depends on the displacement along y and similarly for e_y. Therefore, to facilitate viewing the results, Fig. 8 has been integrated in this manner: we have calculate the average of e_x along direction y for each value of displacement along x, and similarly for the average of e_y along direction x for each value of displacement along y (see Fig. 9). Both error curves appear S-shaped as usual for such an investigation (Amiot *et al.*, 2013), with their minimum located at 0 pixel, 0.5 pixel and 1 pixel. The maximum error is small, about 0.002 pixel; this is essentially due to the transformation of real gray values obtained by

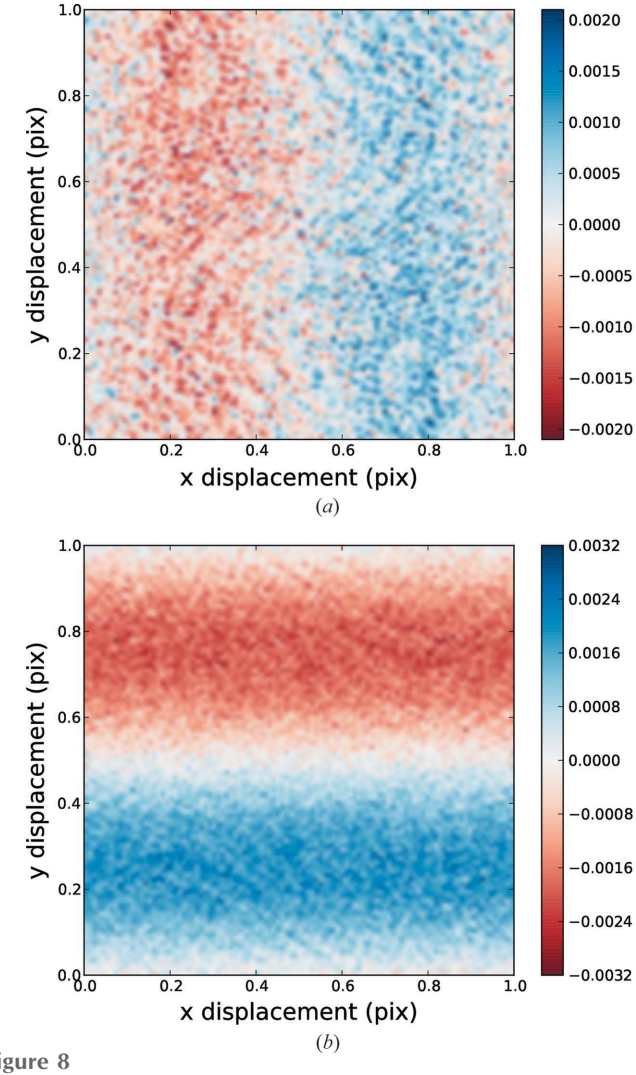

Figure 8
Distribution of errors as a function of displacements i/N pixel and j/N pixel along directions x and y. (*a*) Error e_x and (*b*) error e_y. Displacement errors are expressed in pixel units.

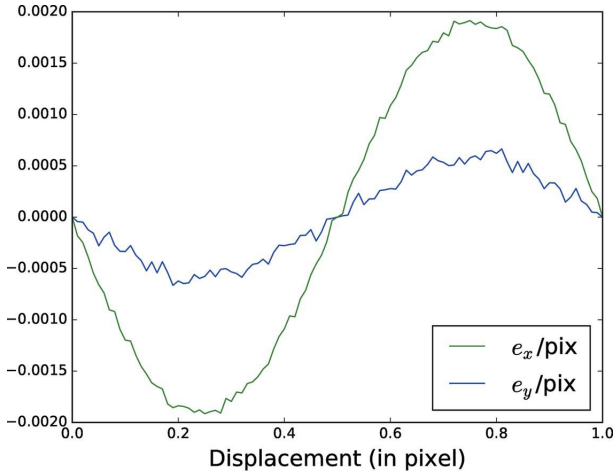

Figure 9
Average errors e_x and e_y for displacement along directions x and y, respectively.

integration of equation (19) into integer ones since the noise is absent in this case.

We performed the same analysis for noisy images. We added random noise to each pixel of the reference and current images, based on the noise model described and identified in §3.2. For each displacement, we generated 100 images since each image will differ due to the random character of the noise that has been added. The discrepancy between the imposed displacement and the average of the measured displacements for the 100 random images is called *systematic error*, while the standard deviation of the measured displacements is called *random error* (Bevington & Robinson, 2002). Fig. 10 depicts the averages and standard deviations of errors for all displacements, representing the systematic errors and random errors, respectively.

In terms of systematic errors, one observes again that errors on the estimated displacements along x and y are rather insensitive on the imposed displacements along the orthogonal directions. The amplitude of systematic error e_y, 0.008 pixel, is smaller than e_x, 0.012 pixel. Compared with the case of noiseless spots, the levels of errors increased significantly due to the introduction of noise.

In terms of random errors, the coupling between error direction and displacement direction still turns out to be weak. The amplitude of random error for e_y, 0.014 pixel, is smaller than for e_x, 0.02 pixel. Compared with Fig. 8, the errors increase significantly with the introduction of image noise. Image noise is thus a limiting factor for DIC.

As for noiseless images, we integrated Fig. 10 along directions for which the corresponding error is mostly insensitive, and the results are shown in Fig. 11. In Fig. 11(*a*), it is found that the error curves appear to be much noisier than those of Fig. 9, and they deviate from an S-shape curve. In Fig. 11(*b*), it

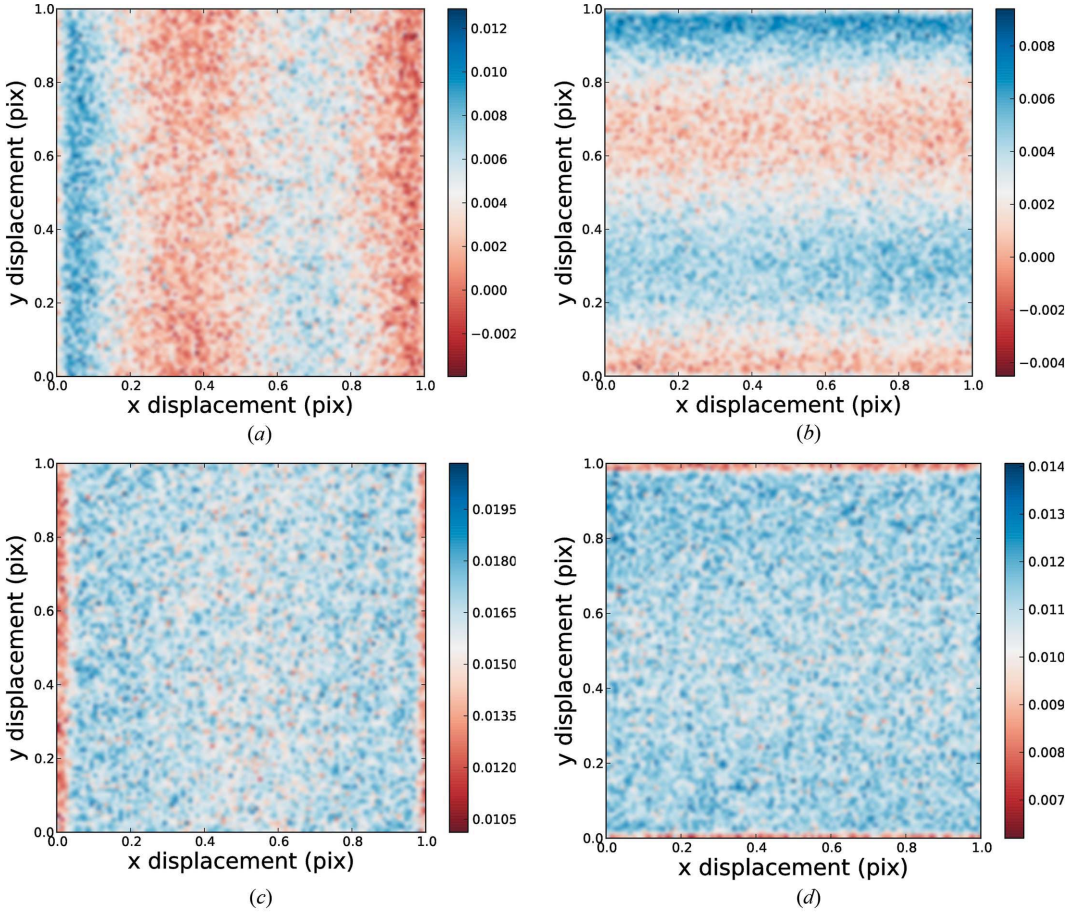

Figure 10
Systematic errors for (*a*) e_x and (*b*) e_y. Random errors for (*c*) e_x and (*d*) e_y. All are in pixels.

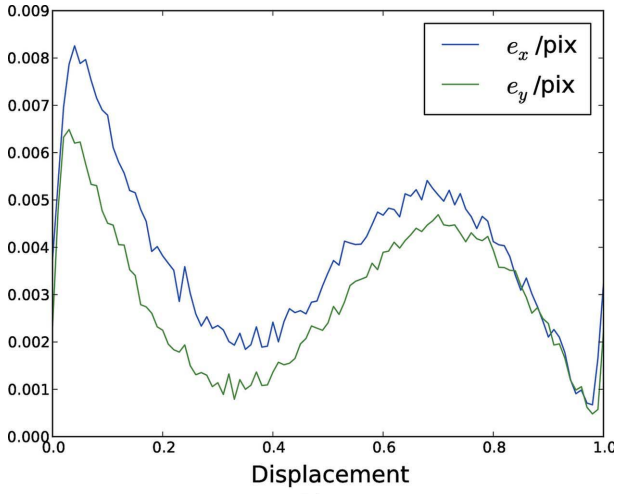

(*a*)

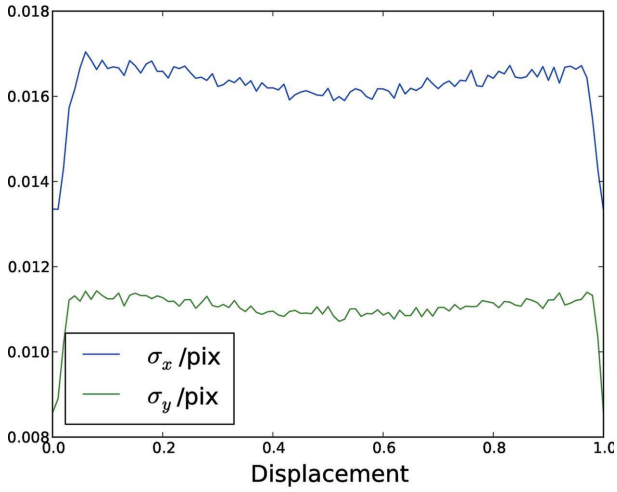

(*b*)

Figure 11
(*a*) Average systematic errors in the x and y directions. (*b*) Average random errors in the x and y directions.

is found that the random errors are smaller near integer pixel displacement, and they quickly reach a plateau as the imposed displacement deviates from an integer pixel. Values of random errors range between 0.01 and 0.02 pixel. DIC errors on displacements along x are systematically larger than those along y, due to a smaller spot width along y leading to larger gray-level gradient (Bornert *et al.*, 2009).

5. The accuracy of Laue-DIC

Now we proceed to analyze the fluctuations of the stress profile in a Si monocrystalline specimen (2.42 mm × 7.97 mm × 35 mm) undergoing *in situ* four-point bending (Fig. 12). The [100], [010] and [001] crystallographic directions of the specimen were aligned along the three edges of the sample, so that symmetries of the applied loading matched the symmetry of sample elastic behavior, thereby reducing so-called out-of-axis effects (Boehler & Sawezuk, 1977) that might generate shear strain. According to Rand & Rovenski (2005), the normal components of the stress should be linearly distributed

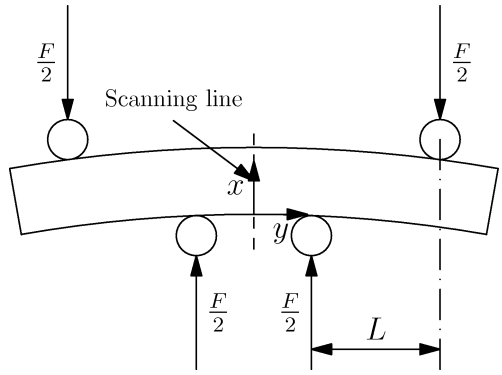

Figure 12
Sketch of the four-point bending test performed on a Si monocrystalline specimen. The line scanned with Laue microdiffraction is indicated. The x and y dimensions are along the thickness (2.42 mm) and length (35 mm) of the specimen, respectively, while the out-of-plane dimension is along the width (7.97 mm) of the specimen.

along the scanning line located in the middle of the sample, and the shear components of the stress should be zero. Nevertheless, the stress profiles of all components in reality exhibit some degree of deviation from linearity due to some possible experimental artefacts such as slight sample misorientation.

Aside from the DIC errors, we will identify other factors that influence the measurement by Laue-DIC, specifically the detector–sample distance. Fig. 13 depicts the stress profiles of the same Si sample bent at a moment of 850 N mm, but the measurements were carried out with different detector–sample distance, namely, 59.8 mm (Fig. 13*a*), 101.7 mm (Fig. 13*b*) and 143.8 mm (Fig. 13*c*). The collected image sequences were treated using the Laue-DIC method to obtain the stress profiles. A larger detector–sample distance theoretically gives a better resolution on spot position, as spots spread on more detector pixels. Meanwhile, fewer spots can be collected on the detector screen as the solid angle captured by the detector decreases. Specifically in this experiment, ∼35, ∼18 and ∼9 spots were collected, respectively, with the three different detector–sample distances. Obviously, the stress profiles turn out to be noisier with larger detector–sample distance.

To investigate in more detail the transmission of image noise and calibration errors to the accuracy of Laue-DIC, we follow a Monte Carlo simulation procedure as stated below:

(i) Fit each spot of the measured LMDI to obtain their parameters A, r_X, r_Y and θ [equation (19)]. This allows having a rough description of spot shape.

(ii) For each spot, use these fitted parameters to generate an artificial spot whose characteristics are similar to the measured spot, and add random noise according to the noise model introduced (§3). A total of 100 random images are generated for each spot.

(iii) Perform Monte Carlo simulations to calculate the systematic and random error of the displacement as described in §4.2. The imposed spot displacement is that estimated by DIC on the real images. This allows the accuracy of the measured displacement to be estimated.

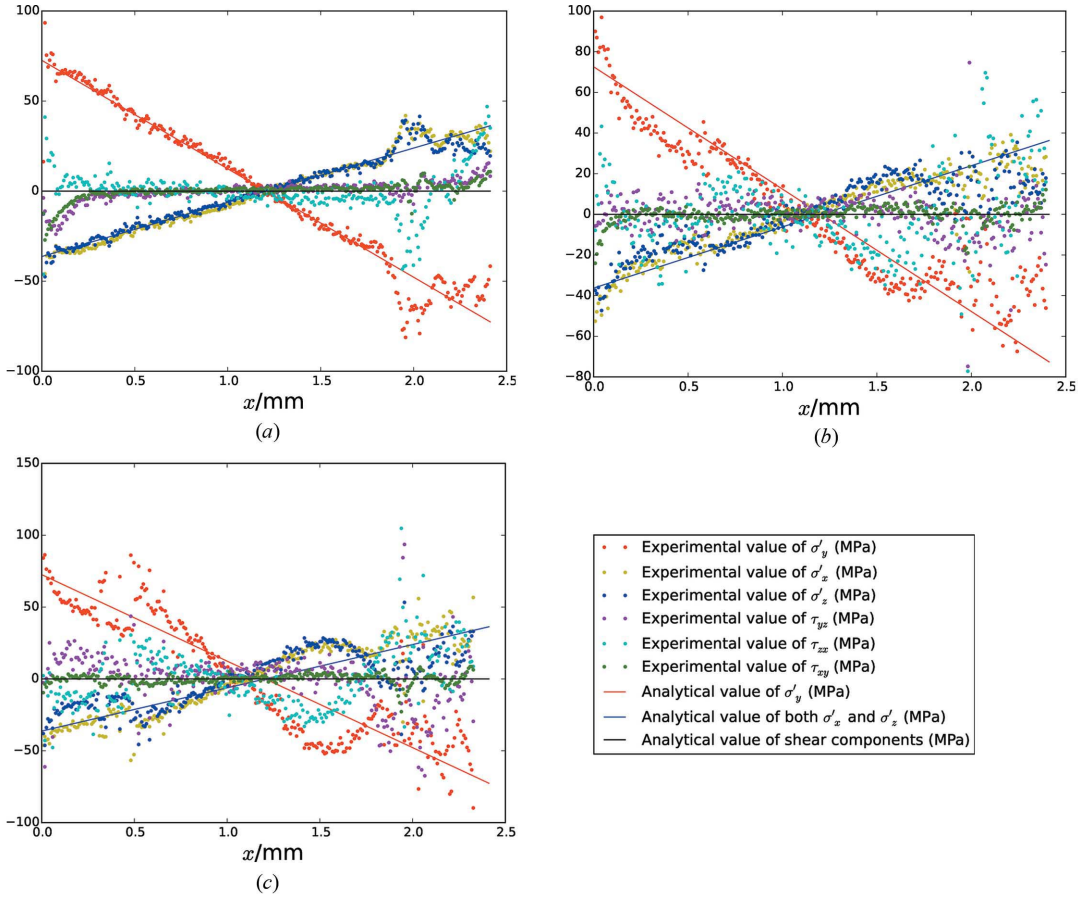

Figure 13
Stress profiles obtained for the bent Si single-crystal at different detector–sample distances: (*a*) 59.8 mm, (*b*) 101.7 mm, (*c*) 143.8 mm.

(iv) For all spots, add to their displacements measured by DIC from real image Gaussian noise, whose means and deviations are the corresponding systematic and random errors estimated from the previous step; on the other hand, add to the calibration parameters (Appendix *A*) the errors estimated by Poshadel *et al.* (2012), which are tabulated in Table 2; and perform statistical tests to calculate the fluctuation of deviatoric stress components, and hence the error bar. The sample size of the statistical tests is also 100.

Error bars obtained with the aforementioned procedure are plotted in Fig. 14 for the stress profiles of Fig. 13(*b*). The half-size of an error bar is the standard deviation of the simulated stress component. It is found that error bars calculated by the proposed procedure are in good quantitative agreement with the observed fluctuations of stress profiles.

6. The collective effect of DIC errors, calibration fluctuations and number of spots considered

In the previous sections, we have qualitatively confirmed the validity of the framework of error estimation. Now, we proceed to use this framework to explore further the collective effect of DIC errors, calibration fluctuations and the number of spots considered upon the evaluation of the deformation gradient **F**. The error on the deformation gradient is defined in the following manner:

Table 2
Uncertainties of the calibration parameters (Poshadel *et al.*, 2012) (pixel size: 31 µm).

σ_d (mm)	σ_{x_c} (pixel)	σ_{y_c} (pixel)	σ_β	σ_γ
0.004	0.16	0.26	0.005°	0.005°

(i) Rescale each component of **F** by the cube root of the determinant of **F** in order to get rid of the unknown volume of the crystal lattice, *i.e.*

$$\hat{\mathbf{F}} \doteq \frac{\mathbf{F}}{(\det \mathbf{F})^{1/3}}. \tag{21}$$

(ii) The error on **F** is defined as

$$\varepsilon_F \doteq \frac{\sum_{i=1}^{3}\sum_{j=1}^{3} |\hat{F}_{ij}^{\rm cal} - \hat{F}_{ij}^{\rm exa}|}{9}, \tag{22}$$

where the superscript 'cal' represents the calculated value after having added noise and performed DIC, and the superscript 'exa' represents the exact prescribed value.

In the case of statistical tests where multi-random cases are treated, we define the systematic error $\overline{\varepsilon}_F$ and random error σ_F on **F** as

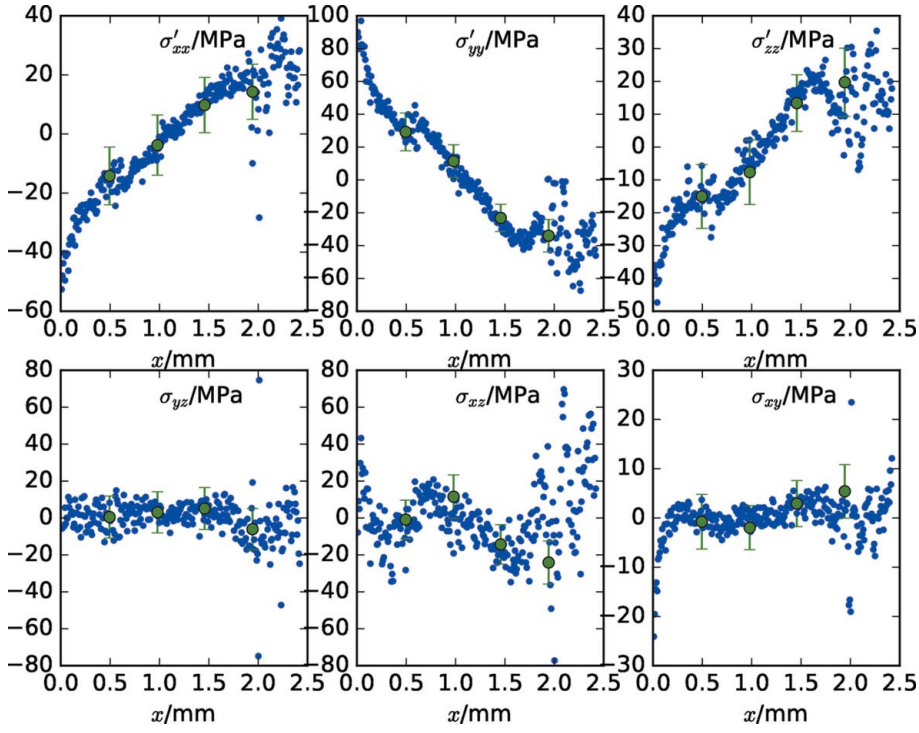

Figure 14
Estimation of the error bars of the stress profiles of Fig. 13(*b*), perform by Monte Carlo simulation.

$$\overline{\varepsilon}_{\mathrm{F}} \doteq \frac{\sum_{i=1}^{3}\sum_{j=1}^{3}|\overline{\hat{F}}_{ij}^{\mathrm{cal}} - \hat{F}_{ij}^{\mathrm{exa}}|}{9}, \qquad \sigma_{\varepsilon_{\mathrm{F}}} \doteq \frac{\sum_{i=1}^{3}\sum_{j=1}^{3}\sigma_{\hat{F}_{ij}^{\mathrm{cal}}}}{9}, \tag{23}$$

where the overline means the average and the σ on the right-hand side of the equation means the standard deviation.

The procedure of the Monte Carlo simulation goes as follows (see Fig. 15, where the superscript 'dis' means the values disturbed by noise):

(i) Give the lattice matrices and calibration parameters of both reference (D^{exa}, $X_{\mathrm{c}}^{\mathrm{exa}}$, $Y_{\mathrm{c}}^{\mathrm{exa}}$, B^{exa}, Γ^{exa}) and current (d^{exa}, $x_{\mathrm{c}}^{\mathrm{exa}}$, $y_{\mathrm{c}}^{\mathrm{exa}}$, β^{exa}, γ^{exa}) configurations.

(ii) Deviate the calibration parameters of the current configuration slightly from their values according to normal distribution with given deviations.

(iii) Calculate the spots' displacements according to a prescribed lattice strain and rotation, and add noise to these exact displacements to represent DIC errors.

(iv) Use the spots' displacements to calculate the relative deformation gradient $\mathbf{F}^{\mathrm{cal}}$, and compare it with the exact prescribed value $\mathbf{F}^{\mathrm{exa}}$.

In our Monte Carlo simulation, we use real data from one of our measurements as input values to make these tests more realistic. The exact values for calibration parameters are listed in Table 3, and the exact values for $\mathbf{M}_0$ are

Table 3
Exact values of calibration parameters in Fig. 15.

d (mm)	x_{c} (pixel)	y_{c} (pixel)	β	γ
59.799	1365.75	943.97	0.344°	0.517°

$$\mathbf{M}_0 = \begin{bmatrix} 1 & -7.74\times10^{-3} & 1.66\times10^{-2} \\ 8.03\times10^{-3} & -0.654 & -0.758 \\ 1.61\times10^{-2} & 0.758 & -0.653 \end{bmatrix}. \tag{24}$$

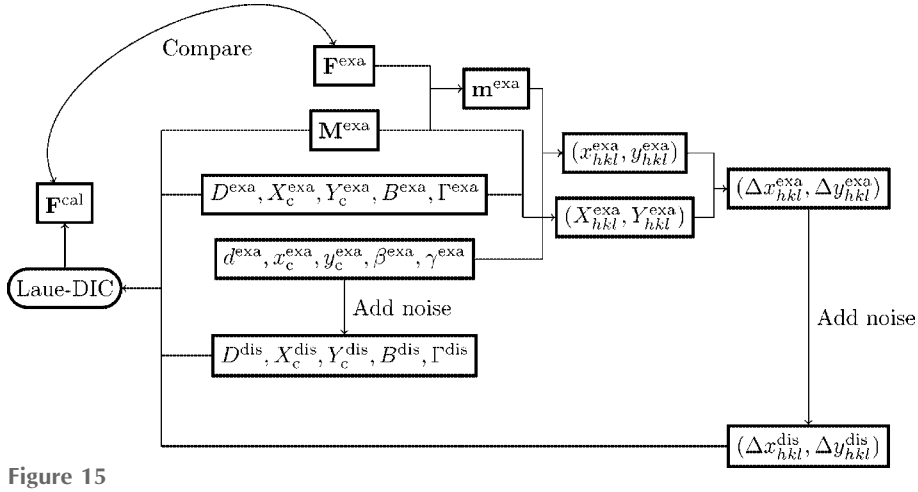

Figure 15
Flowchart of the Monte Carlo simulation.

We considered three deformation cases denoted as I, II and III, for which the relative deformation gradients are given by $\mathbf{F}^{\mathrm{I}} = \mathbf{F}$, $\mathbf{F}^{\mathrm{II}} = \mathbf{F}\cdot\mathbf{F}$ and $\mathbf{F}^{\mathrm{III}} = \mathbf{F}\cdot\mathbf{F}\cdot\mathbf{F}$, respectively, with the exact value for $\mathbf{F}$ being

$$\mathbf{F} = \begin{bmatrix} 1 & 3.33\times10^{-4} & -3.55\times10^{-4} \\ 9.15\times10^{-6} & 1 & -4.49\times10^{-4} \\ -3.36\times10^{-4} & 2.42\times10^{-4} & 1 \end{bmatrix}. \quad (25)$$

The three cases represent increasing the deformations and the rotations in a row. For each case, we tested three subcases, in which the numbers of Laue spots captured by the detector area were 40, 25 and 10, respectively. In the following, the variation of $\mathbf{F}^{\mathrm{cal}}$ is investigated with respect to the various errors listed above.

Variations of $\mathbf{F}^{\mathrm{cal}}$ *measurement with DIC errors.* Here, we will add zero-mean Gaussian errors to the spots' displacements to investigate the influence of DIC errors upon the measurement of $\mathbf{F}^{\mathrm{cal}}$. We will impose all the input displacements of spots in the same Laue image with zero-mean Gaussian errors whose deviations are 0.005, 0.01, 0.015, 0.02, 0.025, 0.03, 0.035, 0.04, 0.045 and 0.05 pixel (from §4 we know that the average error is of the order of 0.015 pixel). Uncertainties of the calibration parameters are tabulated in Table 2. For each deviation level, we generated 500 random cases and then calculated the average errors of lattice matrices.

Variations of $\mathbf{F}^{\mathrm{cal}}$ *measurement with calibration errors.* Similarly, we vary the level of calibration errors by scaling the deviations of all calibration parameters tabulated in Table 2 by a unique scaling factor denoted α. The scaling factor α is set to 0, 0.25, 0.5, 0.75, 1, 1.25, 1.5, 1.75, 2, 2.25, 2.5. In other words, $\alpha = 0$ corresponds to the case for which calibration parameters are perfectly known, while $\alpha = 2$ corresponds to an uncertainty on the calibration parameters that are twice that indicated in Table 2. For the sake of brevity, we only consider the case for which the deviations of the spots' displacements are 0.01 pixel along both the x and y directions, for all spots. The other settings of tests are the same as previously.

The variations of systematic and random errors with imposed zero-mean Gaussian noise are displayed in Fig. 16, and those with the level of calibration errors α are displayed in Fig. 17 (here, for conciseness, only results of case II are displayed; very similar results are observed for cases I and III). In both figures, calculations have been performed with Laue images containing 10, 25 and 40 Laue spots, which are randomly chosen from all indexed spots. These results suggest the following remarks:

(i) Both systematic and random errors of $\mathbf{F}$ decrease when increasing the number of Laue spots. The effect on systematic errors is particularly strong. This result is consistent with Fig. 13, showing that, at larger detector–sample distance, fewer spots are recorded and the stress profiles turn out to be more scattered despite a better resolution of each spot. This result justifies the usual strategy of using as many spots as possible to have a reliable measurement of stress, thereby putting the detector close to the specimen to collect more spots, or alternatively having a larger detection surface.

(ii) Systematic errors on $\mathbf{F}$ increase abruptly with instilling the zero-mean Gaussian errors either to the spots' displacements or to the calibration parameters. However, the systematic errors become stable with further increasing the deviation of errors.

(iii) Random errors only slightly increase with increasing the errors on the spots' displacements. In contrast, random errors are strongly correlated with the uncertainty on calibration parameters; they are found to depend almost linearly on the scaling factor α.

(iv) Random errors seem essentially insensitive to the prescribed deformation gradient (cases I, II and III provide very similar results). Systematic errors seem to be more affected but in a complex way; they globally decrease from case I to case III, but this is not general, as case II in Fig. 17 show smaller errors than case III, which is not shown for conciseness.

(v) The systematic and random errors on $\mathbf{F}$ are of the order of 10^{-4}, well adapted for micromechanical studies.

As mentioned above, random errors seem to increase linearly with the scaling factor α, while they seem to be more stable with the deviations of the displacement errors. This may indicate that, for the investigated case, the dominant factor governing the random errors should be the scaling factor α. This may lead us to postulate that the displacement errors may dominate calibration errors, for larger displacement errors. To prove this point, we further extend the range of the abscissa of Figs. 16(b), 16(d) and 16(f) to 0.16 pixel. We then plot in Fig. 18 the error curves for multiple values of α, with respect to the displacement error. To save space, we only consider here case II ($\mathbf{F}^{\mathrm{II}} = \mathbf{F}\cdot\mathbf{F}$) with 25 spots on the Laue image (the set of 25 spots is different from that adopted in Figs. 16 and 17).

In Fig. 18, it is obvious that all curves asymptotically converge to a certain curve if we further increase the deviations of displacement errors. For $\alpha = 0$, *i.e.* when calibration parameters are exactly given, the errors increase linearly with the DIC errors. As we increase α, a basin is formed in which the error on $\mathbf{F}$ increases slightly with the displacement errors, and the width of this basin increases with α. This implies that, when the accuracy of the spot displacement is good (*e.g.* as obtained with DIC for intense peaks), improvement of the measurement of $\mathbf{F}$ essentially requires a better knowledge of the calibration parameters (smaller α). On the other hand, when spot displacements are poorly determined (*e.g.* when a complex spot shape is fitted with simple analytical functions, or when the spot shape changes between the reference and the deformed image), a better calibration knowledge barely improves the measurement of $\mathbf{F}$. Coming back to our experiments with $\alpha = 1$ and average DIC error of 0.015 pixel, it is clear that the current bottleneck of Laue-DIC is the estimation of the calibration parameters. With respect to this result, an enhanced version of the Laue-DIC method has been proposed to neutralize the effect of the uncertainties of calibration parameters (Zhang *et al.*, 2015). In this method, the calibration parameters are to be optimized alongside the elastic strain and lattice orientation. Nevertheless, Laue-DIC and enhanced Laue-DIC methods can give comparable results

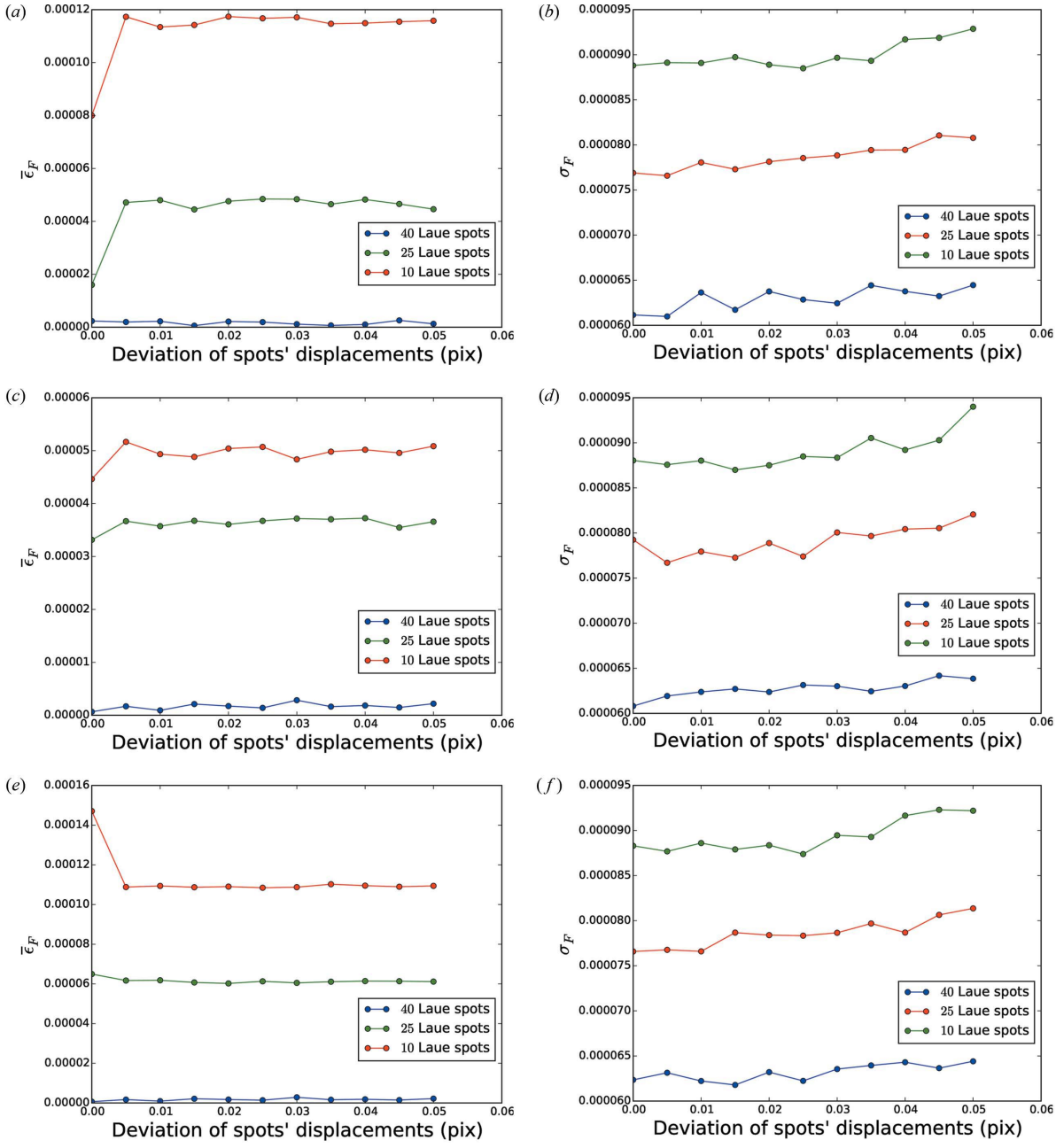

Figure 16
Influence of imposed zero-mean Gaussian errors on spots' displacements onto the measurement of $\mathbf{F}^{\text{cal}}$. (Left) Systematic errors. (Right) Random errors. (a, b) Case I, (c, d) case II, (e, f) case III. Results for $\alpha = 1$.

of stress when the calibration parameters are fairly estimated, with much less CPU time for the initial method than its enhanced version.

7. Summary

In this paper we have presented a framework for estimating the error of the Laue-DIC method by Monte Carlo simulation. First we have proposed a simple procedure to characterize the image noise by linear regression, and it turned out that the measured statistical properties of the image noise are well reproduced by a simple Poisson–Gauss noise model. The detector gain for each pixel is not found to depend significantly on the X-ray beam energy.

The estimated image noise is then fed into a Monte Carlo model which consists of the following two steps:

(i) Generate a synthetic spot with realistic size, add image noise to the spot using the identified Poisson–Gauss model, and perform a statistical inverstigation to estimate the DIC errors. With this procedure, one can estimate that the displacement error for DIC is better than 0.02 pixel for typical Laue images (random error).

(ii) Account for the DIC errors and calibration errors for the calculation of the deformation gradient $\mathbf{F}$ in order to

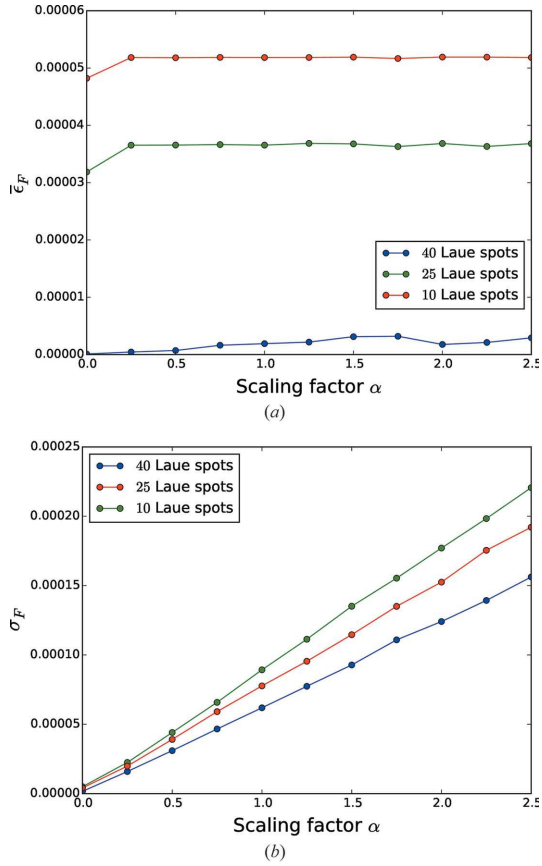

Figure 17
Influence of perturbations of calibration parameters α onto the measurement of $\mathbf{F}^{\text{cal}}$ for case II. (*a*) Systematic errors. (*b*) Random errors. Results for a noise of 0.01 pixel on a spot's displacement.

estimate its resulting uncertainty. For an *in situ* deformed Si single-crystal, the uncertainty on the deformation gradient is estimated to be of the order of 10^{-4}.

This proposed method quantitatively reproduces the fluctuations of the stress profiles for the bent Si single-crystal (see Fig. 14), attesting the validity of the approach.

We also applied this method to explore the collective effect of DIC errors, calibration errors and the number of Laue spots used for lattice strain estimation. The following conclusions have been demonstrated:

(i) Increasing the number of Laue spots for lattice strain estimation remarkably improves the measurement of the deformation gradient, although this benefit comes at the expense of a poorer resolution on spot shapes.

(ii) The systematic error of Laue-DIC seems to be stable with the DIC error and α, the scaling factor of the calibration error.

(iii) The random errors of Laue-DIC can be considered as a function of DIC and calibration errors. Several error regimes can be identified. (*a*) When calibration errors (α) are small enough, the error on spot displacement from DIC constitutes the dominant factor, and the error on **F** increases linearly with the DIC error. (*b*) If calibration errors (α) are gradually increased, the random error on **F** becomes less sensitive to the DIC error, and in that case the calibration error constitutes the dominant factor.

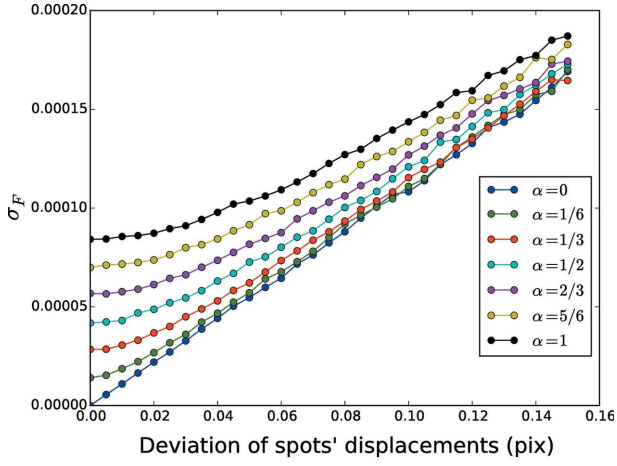

Figure 18
Variation of error curves with scaling factor α and displacement errors.

APPENDIX *A*
The geometry of Laue microdiffraction

The setup of Laue microdiffraction can be described by five parameters (Ulrich *et al.*, 2011). These parameters are defined in Fig. 19: d is the distance from the illuminated position O (intersection of the incident beam with the specimen surface) to the detector; $\overrightarrow{\text{OP}}$, together with the direction of the incident beam, defines a laboratory frame $\Re$, in which $\mathbf{e}_y$ is the unit vector of the y-axis which is codirectional with the incident beam. $\mathbf{e}_x$, the unit vector of the x-axis, is defined as

$$\mathbf{e}_x \doteq \frac{\mathbf{e}_y \times \overrightarrow{\text{OP}}}{\|\mathbf{e}_y \times \overrightarrow{\text{OP}}\|}, \tag{26}$$

and $\mathbf{e}_z$, the unit vector of the z-axis, is defined as

$$\mathbf{e}_z \doteq \mathbf{e}_x \times \mathbf{e}_y; \tag{27}$$

β is the angle between $\mathbf{e}_z$ and $\overrightarrow{\text{OP}}$, γ is the rotation angle of the area detector around $\overrightarrow{\text{OP}}$; x_c and y_c are the distances of P to two perpendicular edges of the area detector. Pixels on the detector are assumed to be arranged in a perfect square array with a known step, *i.e.* any error resulting from the distortion

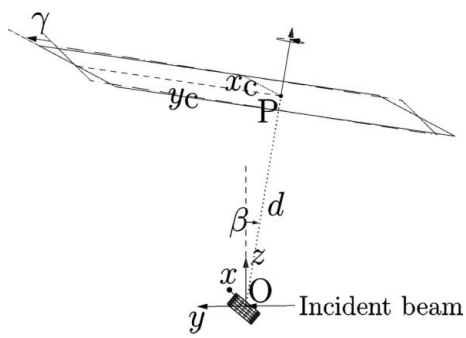

Figure 19
Calibration parameters that define the geometry of the experimental setup.

of pixels has been corrected by certain algorithms (Paciorek *et al.*, 1999; Hülsen *et al.*, 2005).

The five parameters (d, x_c, y_c, β, γ) are necessary to calculate the elastic strain and the orientation because they serve to translate any rectangular coordinate on the area detector to its angular coordinate in $\Re$, and *vice versa*,

$$\mathbf{X} \overset{(d,x_c,y_c,\beta,\gamma)}{\rightarrow} \mathbf{n}, \tag{28}$$

where $\mathbf{X} = [x, y]^T$ is a rectangular coordinate on the area detector and $\mathbf{n}$ is the unit vector pointing from the origin of $\Re$, *i.e.* O, to $\mathbf{X}$. In this paper, we denote $\mathcal{C}$ as the set of five calibration parameters.

APPENDIX *B*
Dependence of gain γ on photon energy

Each Laue spot for a lattice plane (*hkl*) is generated by photons with a certain energy, E_{hkl}. It is natural to suppose that the gain γ of the detector depends on the energy of the incident X-rays. E_{hkl} is inversely proportional to the wavelength according to the de Broglie relation,

$$E_{hkl} = \frac{2\pi\hbar c}{\lambda_{hkl}}, \tag{29}$$

where the subscript '*hkl*' represents the index of the lattice plane from which the spot is diffracted, $\hbar$ is the reduced Planck's constant and c is the light speed. Substituting equation (1) into (29), we have

$$E_{hkl} = \frac{\pi\hbar c}{d_{hkl}\sin\theta}, \tag{30}$$

where d_{hkl} is the d-spacing of the lattice plane. For a cubic lattice, d_{hkl} is given as

$$d_{hkl} = \frac{a}{(h^2+k^2+l^2)^{1/2}}, \tag{31}$$

where a is the side length of the cubic lattice. Therefore, for a cubic lattice, the energy of a photon diffracted by the (*hkl*) lattice plane is

$$E_{hkl} = \frac{\pi\hbar c(h^2+k^2+l^2)^{1/2}}{a\sin\theta}. \tag{32}$$

For all spots under consideration, we have thus plotted in Fig. 20 the relation between γ and E_{hkl}. In this figure, we do not see any clear correlation between spot energy E and gain γ and therefore we could only estimate the range of gain from it. Nevertheless, the gain is most likely to be constant with varying spot energy since the scintillator of the CCD detector is designed to absorb all photons in the energy range (~5–25 keV). Hence, in this work we will take the average value, $\gamma = 0.125$, to estimate the error of Laue-DIC.

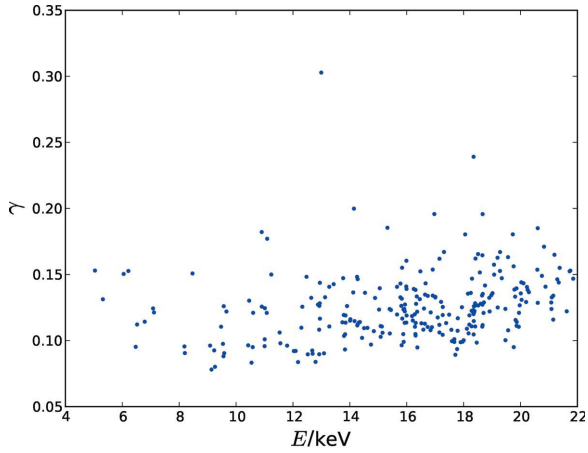

Figure 20
Energy of the incident X-ray beam *versus* estimated detector gain γ. Each point corresponds to a Laue spot.

Acknowledgements

We are very grateful to J. P. Vassali (ESRF) for his help on sample preparation, and to O. Robach and J. S. Micha (CEA and ESRF) for their help in performing microdiffraction experiments at BM32 and their very fruitful comments on this work. We also acknowledge financial support provided by the French ANR agency (MICROSTRESS project, ANR-11-BS09-030) and the China Scholarship Council.

References

Abanto-Bueno, J. & Lambros, J. (2002). *Eng. Fracture Mech.* **69**, 1695–1711.

Amiot, F., Bornert, M., Doumalin, P., Dupré, J.-C., Fazzini, M., Orteu, J. J., Poilâne, C., Robert, L., Rotinat, R., Toussaint, E., Wattrisse, B. & Wienin, J. S. (2013). *Strain*, **49**, 483–496.

Arndt, U. W. & Gilmore, D. J. (1979). *J. Appl. Cryst.* **12**, 1–9.

Barabash, R., Ice, G. E., Larson, B. C., Pharr, G. M., Chung, K.-S. & Yang, W. (2001). *Appl. Phys. Lett.* **79**, 749–751.

Bergonnier, S., Hild, F. & Roux, S. (2005). *J. Strain Anal. Eng. Des.* **40**, 185–197.

Bevington, P. R. & Robinson, D. K. (2002). *Uncertainties in Measurements*, pp. 1–16. New York: McGraw-Hill.

Boehler, J. & Sawezuk, A. (1977). *Acta Mech.* **27**, 185–206.

Bornert, M., Brémand, F., Doumalin, P., Dupré, J.-C., Fazzini, M., Grédiac, M., Hild, F., Mistou, S., Molimard, J., Orteu, J.-J., Robert, L., Surrel, Y., Vacher, P. & Wattrisse, B. (2009). *Exp. Mech.* **49**, 353–370.

Bornert, M., Doumalin, P., Dupré, J.-C., Poilane, C., Robert, L., Toussaint, E. & Wattrisse, B. (2017). *Opt. Lasers Eng.* **91**, 124–133.

Bornert, M., Valès, F., Gharbi, H. & Nguyen Minh, D. (2010). *Strain*, **46**, 33–46.

Castelnau, O., Drakopoulos, M., Schroer, C., Snigireva, I., Snigirev, A. & Ungár, T. (2001). *Nucl. Instrum. Methods Phys. Res. A*, **467–468**, 1245–1248.

Chung, J.-S. & Ice, G. E. (1999). *J. Appl. Phys.* **86**, 5249–5255.

Doumalin, P. & Bornert, M. (2000). *Interferometry in Speckle Light*, pp. 67–74. Berlin/Heidelberg: Springer.

Ferrié, E., Buffière, J.-Y. & Ludwig, W. (2005). *Int. J. Fatigue*, **27**, 1215–1220.

He, B. B. (2009). *X-ray Detectors*, pp. 85–132. New York: John Wiley and Sons, Inc.

Hofmann, F., Eve, S., Belnoue, J., Micha, J. & Korsunsky, A. (2011). *Nucl. Instrum. Methods Phys. Res. A*, **660**, 130–137.

Hülsen, G., Brönnimann, Ch. & Eikenberry, E. (2005). *Nucl. Instrum. Methods Phys. Res. A*, **548**, 540–554.

Magid, K., Florando, J., Lassila, D., LeBlanc, M., Tamura, N. & Morris, J. W. Jr (2009). *Philos. Mag.* **89**, 77–107.

Nguyen, V. P., Stroeven, M. & Sluys, L. J. (2011). *J. Multiscale Model.* **3**, 229–270.
Ohashi, T., Barabash, R., Pang, J., Ice, G. & Barabash, O. (2009). *Int. J. Plast.* **25**, 920–941.
Paciorek, W. A., Meyer, M. & Chapuis, G. (1999). *J. Appl. Cryst.* **32**, 11–14.
Peters, W. H. & Ranson, W. F. (1982). *Opt. Eng.* **21**, 427–431.
Petit, J., Castelnau, O., Bornert, M., Zhang, F. G., Hofmann, F., Korsunsky, A. M., Faurie, D., Le Bourlot, C., Micha, J. S., Robach, O. & Ulrich, O. (2015). *J. Synchrotron Rad.* **22**, 980–994.
Ponchut, C. (2006). *J. Synchrotron Rad.* **13**, 195–203.
Poshadel, A., Dawson, P. & Johnson, G. (2012). *J. Synchrotron Rad.* **19**, 237–244.
Rand, O. & Rovenski, V. (2005). *Analytical Methods in Anisotropic Elasticity*, pp. 215–248. Boston: Birkhäuser.
Robach, O., Micha, J.-S., Ulrich, O. & Gergaud, P. (2011). *J. Appl. Cryst.* **44**, 688–696.
Robach, O., Micha, J.-S., Ulrich, O., Geaymond, O., Sicardy, O., Härtwig, J. & Rieutord, F. (2013). *Acta Cryst.* A**69**, 164–170.
Stanton, M., Phillips, W. C., Li, Y. & Kalata, K. (1992). *J. Appl. Cryst.* **25**, 638–645.
Sutton, M. A., Orteu, J.-J. & Schreier, H. W. (2009). *Image Correlation for Shape, Motion and Deformation Measurements*, ch. 1, pp. 1–12. New York: Springer.
Tamura, N. (2014). *XMAS: A Versatile Tool for Analyzing Synchrotron X-ray Microdiffraction Data*, pp. 125–155. Singapore: World Scientific.
Tamura, N., Celestre, R. S., MacDowell, A. A., Padmore, H. A., Spolenak, R., Valek, B. C., Meier Chang, N., Manceau, A. & Patel, J. R. (2002). *Rev. Sci. Instrum.* **73**, 1369–1372.
Tong, W. (2005). *Strain*, **41**, 167–175.
Ulrich, O., Biquard, X., Bleuet, P., Geaymond, O., Gergaud, P., Micha, J. S., Robach, O. & Rieutord, F. (2011). *Rev. Sci. Instrum.* **82**, 033909.
Ungár, T., Balogh, L., Zhu, Y. T., Horita, Z., Xu, C. & Langdon, T. G. (2007). *Mater. Sci. Eng. A*, **444**, 153–156.
Valek, B. C. (2003). PhD thesis, Standford University, USA.
Wang, Y. & Cuitiño, A. M. (2002). *Int. J. Solids Struct.* **39**, 3777–3796.
Wang, Y. Q., Sutton, M. A., Bruck, H. A. & Schreier, H. W. (2009). *Strain*, **45**, 160–178.
Waterman, D. & Evans, G. (2010). *J. Appl. Cryst.* **43**, 1356–1371.
Wattrisse, B., Chrysochoos, A., Muracciole, J.-M. & Némoz-Gaillard, M. (2001). *Exp. Mech.* **41**, 29–39.
Yamaguchi, I. (1981). *J. Phys. E*, **14**, 1270–1273.
Yan, H. & Noyan, I. C. (2006). *J. Appl. Cryst.* **39**, 320–325.
Zhang, F. G., Castelnau, O., Bornert, M., Petit, J., Marijon, J. B. & Plancher, E. (2015). *J. Appl. Cryst.* **48**, 1805–1817.